Radiation Environment in the Large Hadron Collider During the 2022 Restart and Related RHA Implications

Kacper Biłko, *Graduate Student Member, IEEE*, Rubén García Alía, *Member, IEEE*, Ygor Aguiar, *Member, IEEE*, Salvatore Danzeca, Diego Di Francesca, Simone Gilardoni, Sylvain Girard, *Senior Member, IEEE*, Daniel Ricci, Marc Sebban, and Slawosz Uznanski

***Abstract*— In this work, we present the radiation environment of the large hadron collider (LHC), focusing on the year 2022, the first after the Long Shutdown 2 (LS2) (2019–2021). We highlight the most prominent radiation-level changes with respect to the 2018 operation, commenting on the related Radiation Hardness Assurance implications. In addition to presenting data from well-established radiation monitors, such as beam loss monitors (BLMs) and RadMons, we demonstrated the excellent capabilities of the recently deployed distributed optical fiber radiation sensing (DOFRS) covering selected regions of the LHC. Profiting from the static random access memories (SRAMs) deployed along the accelerator and its shielded alcoves, we demonstrated their capabilities for distributed SEU monitoring.**

***Index Terms*— Beam loss monitors (BLMs), CERN, FGClite, large hadron collider (LHC), optical fiber, radiation hardness assurance, RadMon, single-event effect, total ionizing dose (TID).**

I. Introduction

THE large hadron collider (LHC) [1] at CERN hosts thousands of radiation-exposed electronic systems, with a total of millions of active semiconductor parts. Such systems are critical for the successful operation of the accelerator, which is, therefore, threatened by the stochastic and cumulative radiation effects occurring in its electronic components and systems [2]. In fact, radiation effects on electronics were the main source of accelerator downtime during its first years of operation, in the so-called LHC Run 1, mainly covering the 2011 and 2012 years. This resulted in the need to implement urgent mitigation measures to ensure the fulfillment of the scientific objectives of the accelerator infrastructure. Such measures, coordinated by the radiation to electronics (R2E) project at CERN, mainly consisted of relocating and shielding accelerator equipment sensitive to radiation effects on electronics [3]. In both cases, the mitigation effort, carefully prioritized through radiation level and equipment sensitivity studies, required a significant cost and time investment, mainly due to the associated cabling and civil engineering activities. Such mitigation measures were mainly implemented during the so-called Long Shutdown 1 (2013 and 2014) as well as throughout Run 2 (2015–2018) [3]. These mitigation efforts were complemented by a more systematic approach toward the design and qualification of radiation-tolerant electronics systems, based on commercial-off-the-shelf (COTS) microelectronics components [4]. Except for 2015 [5], the mitigation and prevention (i.e., through radiation-tolerant design and qualification) efforts resulted in an acceptable rate of radiation-induced system failures during Run 2, albeit with an increased impact on 2018 due to a combination of enhanced radiation levels in several critical locations as well as possible cumulative damage contributions. It is worth mentioning at this stage that the radiation effects in electronics affecting the LHC operation typically come in the form of functional interrupts in critical systems that trigger a so-called beam dump, consisting in the safe extraction of the beam from the accelerator, therefore avoiding potential severe damage of the accelerator infrastructure due to inadequate handling of the energy stored in it [6]. In some cases, such functional interrupts can be removed by remotely resetting the concerned equipment. However, other cases require a manual reset or electronic board replacement, adding extra downtime on top of the 2–3 h required to re-establish the stable beam conditions in the LHC and restart the collisions for physics data production. Therefore, to a first approximation, the impact of radiation effects on the availability and performance of the LHC can be measured through the number of beam dumps triggered by radiation effects on electronics. This quantity is typically expressed per unit integrated luminosity, which is proportional to the number of collisions produced in the detector regions of the accelerator. The evolution of this important figure-of-merit throughout Run 2 and Run 3 can be seen in Fig. 1, providing a quantitative view of the qualitative description above.

After the Long Shutdown 2 (LS2) period (2019–2021), 2022 has witnessed the restart of the LHC, in what has been the first year of the Run 3 period, which is expected

Manuscript received 21 July 2023; revised 6 October 2023 and 25 October 2023; accepted 25 October 2023. Date of publication 27 October 2023; date of current version 18 April 2024.

Kacper Biłko is with CERN, 1211 Geneva, Switzerland, and also with Laboratoire Hubert Curien, CNRS UMR 5516, Université Jean Monnet, 42000 Saint-Étienne, France (e-mail: kacper.bilko@cern.ch).

Rubén García Alía, Ygor Aguiar, Salvatore Danzeca, Diego Di Francesca, Simone Gilardoni, Daniel Ricci, and Slawosz Uznanski are with CERN, 1211 Geneva, Switzerland.

Sylvain Girard is with Universite Jean Monnet, 42000 Saint-Étienne, France and also with Institut Universitaire de France (IUF), Ministère de l'Enseignement Supérieur et de la Recherche, 75231 Paris, France.

Marc Sebban is with Université Jean Monnet, 42000 Saint-Étienne, France.

Color versions of one or more figures in this article are available at https://doi.org/10.1109/TNS.2023.3328145.

Digital Object Identifier 10.1109/TNS.2023.3328145

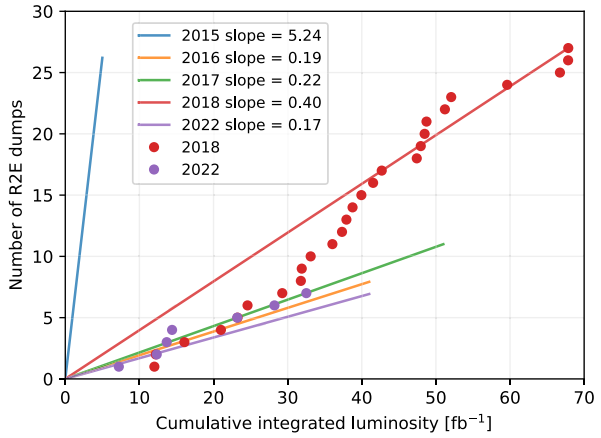

Fig. 1. R2E-induced beam dump events as a function of the integrated luminosity for the CMS experiment. Additionally, for 2018 and 2022, each R2E-induced beam dump is depicted as a point. The slopes are given by the total number of dumps per the integrated luminosity (for ATLAS/CMS experiments).

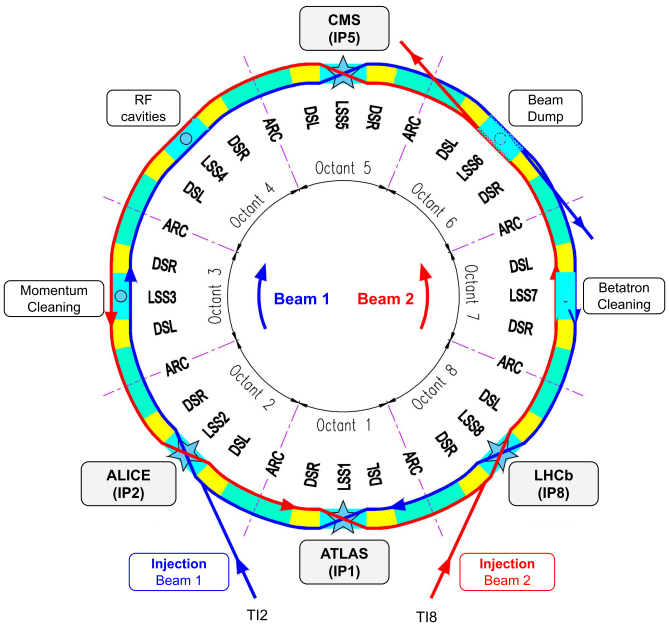

Fig. 2. Layout of the LHC with the two counter circulating beams. Adapted from [11].

to last until 2025, included. From an R2E perspective, the accelerator restart provides a very challenging and interesting context, owing mainly to: 1) the changes in the radiation levels linked to accelerator upgrades and modification of its operating conditions; 2) the aging (radiation and nonradiation) of the installed electronics systems; 3) the introduction of new radiation-exposed systems within the accelerator infrastructure; and 4) deployment of the new radiation monitoring solutions such as distributed optical fiber radiation sensor (DOFRS) [7], with already demonstrated excellent capabilities in the smaller CERN accelerators [8], [9]. Therefore, in this article, we will describe the status and outlook of the LHC radiation environment and its effects, as per the feedback from 2022, the first year of the Run 3 operation.

The article is structured as follows. Section II presents the layout of the accelerator with the available radiation monitoring infrastructure. The section also gives insights into the LHC operation and electronics systems exposed to radiation.

In Section III, the radiation levels measured in the LHC in 2022 are described, putting them in contrast with the Run 2 experience, and focusing on 2018, the last year before LS2. Moreover, the section analyzes the 2022 LHC operation from a component-level radiation effects perspective, making use of Single Event Upset data in static random access memories (SRAMs) present in a highly distributed system across the LHC, and putting it in the context of the radiation environment.

Section IV summarizes the 2022 LHC experience related to system-level radiation effects having impacted the operation of the accelerator, linking the observations at the component level, as well as the radiation monitor measurements. This section also provides feedback on the operation of radiation-tolerant systems installed during LS2. Section V provides a summary of Sections II–IV, as well as an outlook of the LHC radiation environment and effects for the rest of Run 3 and the high-luminosity LHC (HL-LHC) era (i.e., as of 2029 onward) [10].

II. LHC: Layout and Radiation Monitoring

A. Accelerator Layout

The LHC has a circumference of nearly 27 km and consists of eight insertion regions (IRs), that are interconnected with eight arc sections, through the dispersion suppressor (DS) regions [11]. A schematic drawing of the LHC is illustrated in Fig. 2.

Each IR host, in its center, is either an experiment or a system essential for the accelerator operation (e.g., collimators). The LHC is arranged in so-called half-cells defined by the main quadrupole magnets. For example, the DS region starts in the 8th and ends in the 11th half-cell (inclusive). The arc spans between the 12th half-cells (numbering until 34th) of two neighboring IRs.

The role of DS regions is to interconnect and match the beam optics between a center of an IR region and an arc, by reducing the horizontal beam dispersion through dedicated magnet settings. Arc sectors, through the dipole magnets, are responsible for the bending and transport of beams between IRs.

IR1 hosts the ATLAS experiment [12], one of the two high-luminosity experiments. The second one, CMS, is installed in IR5 [13]. Additionally, LHC houses two smaller experiments, ALICE [14] and LHCb [15], located at the center of IR2 and IR8, respectively.

The remaining four IRs are not hosting experiments but are critical for the operation of the accelerator. IR3 and IR7 contain collimators [16], used to remove particles that do not meet the desired acceptance in terms of momentum (IR3) or transverse position (IR7). IR4 is responsible for beam acceleration, hosting radio-frequency cavities [17], and multiple other beam instruments [18]. IR6 functionality is dedicated to the beam dump system, allowing for a safe beam extraction [19].

TABLE I
SUMMARY OF THE LHC RADIATION MONITORS EXPLOITED IN THIS STUDY WITH THEIR MAIN PROPERTIES

	DOFRS	BLM	RadMon
# of units	continuous	3513	235
Spatial res.	≥ 1 m	discrete	discrete
Time res.	~ 8 h	40 μs	$\sim$hour
annual. TID det. range	1 Gy-1 kGy	10 mGy-1 MGy	1 Gy-200 Gy
Distance (m): Horiz./Vert.	0/1.55 (IR1) 0/1.25 (IR5) 0/1.25 (IR7)	0.5/0 (side) 0/0.5 (top)	0/-0.7
Measurand	TID (SiO_2)	TID (air)	TID (SiO_2), 1-MeV-Si-n-eq, HEH-eq th-n-eq

B. LHC Radiation Monitoring

The main system used to assess radiation levels along the LHC is composed of beam loss monitors (BLMs), measuring total ionizing dose (TID). In several locations, these measurements are supported by dedicated CERN monitors, RadMons, providing the complete characterization of the mixed radiation field from an R2E perspective. Recently, during LS2, several locations of the LHC were equipped with DOFRS, allowing for a continuous distributed TID measurement. The capabilities of the monitors are listed in Table I.

1) Beam Loss Monitors: In most of the accelerator locations, beam losses are expected, their origins are well understood, and components are designed to withstand them. For its monitoring, a dedicated Beam Loss Monitoring system has been designed and deployed along the accelerator [20], [21], [22], [23]. The core is 3600 ionization chambers, BLMs. In the case of unexpected behavior (e.g., once the acceptable beam loss threshold is exceeded), within a single beam turn (89 μs), thanks to the interlock system, the beam is safely extracted from the accelerator and disposed of at the dedicated dump blocks, designed to cope with the enormous deposition power. Although not designed primarily for dosimetry, after a dedicated data processing [24], BLMs provide very detailed information about TID distribution and time evolution along the accelerator [25].

2) RadMon: The RadMon is a CERN-developed solution, based on COTS components, to characterize the radiation environment, not only in terms of TID, but also displacement damage and SEUs [26], [27]. Through the combination of different SRAM memories and based on the SEEs, an equivalent fluence of high-energy hadrons (HEHeq) [28] and thermal neutrons (th-n-eq) are retrieved [29]. There are over 300 RadMon units distributed along the accelerator and in the shielded alcoves containing electronic systems, whereas, in this study, only data from the LHC tunnel and RR shielded alcoves are presented.

3) DOFRS: As of 2021, selected locations in the accelerator (namely the DSs of IR1, IR5, and IR7) are equipped with DOFRS [30]. The core of the system is P-doped silica optical fiber allowing TID measurements through the Radiation-Induced-Attenuation mechanism [31]. The system allows for a continuous TID profile measurement over several hundreds of meters, similar to the CERN injectors, namely the Proton Synchrotron Booster, the Proton Synchrotron, and the super proton synchrotron (SPS). In the DSs, the fiber has a fairly constant relative position with respect to the accelerator.

C. LHC Operation Statistics

The LHC is operated in fills, with each fill being defined as the period between the first beam injection and extraction. A typical LHC fill, depicted in Fig. 3, consists of several beam injections from the SPS, happening with a beam energy of 450 GeV. Later, after the accomplished injection phase, the beam is accelerated (ramped up) up to almost 7 TeV (6.5 TeV in 2018 and 6.8 TeV in 2022). At the top energy, the accelerator is adjusted to provide colliding beams to the four experiments. Once the intensity or quality of beams is no longer optimal, or in the case of an issue, the beams are extracted (dumped) from the accelerator and disposed of on the dump blocks around IR6.

The statistics of the 2022 operation, when compared to 2018, are presented in Table II. In a nutshell, operation in 2022 achieved approximately 60% what was delivered in 2018 in terms of integrated intensity or integrated experiment luminosity (62%). Therefore, the 2022 radiation levels in multiple locations in the LHC are expected to be approximately 60% of what was measured in 2018.

It is worth noting that 2022 was a recommissioning year, hence even if the number of injected protons was close to 2018's value (90%), a significant fraction of the operation was not devoted to physics experiments. An example of this is the scrubbing operation (high intensity at the injection energy) aiming at improving the accelerator vacuum and surface quality, as reflected in the ratio (2022 versus 2018) of the total number of protons dumped (96%) or lost in collimation regions (81%). Fills with collisions at the experiments corresponded to 63% of 2018's injected intensity (collision fills only).

During a fill with collisions the intensity in the accelerator decreases primarily due to: 1) p–p interactions at the experiments (luminosity burn-off, $\sigma = 72$ mb [32]); and 2) beam cleaning at the collimators in IR7 (dominant) and IR3, as given by the following equation:

$$\text{injected} - \text{dumped} \approx \text{luminosity burn-off} + \text{cleaned in IR7(3)}. \quad (1)$$

The other losses, for example, due to beam–residual gas interactions are minor and are shadowed by the luminosity burn-off/collimation losses.

D. Exposed Electronic Systems

A complex accelerator such as the LHC requires an important number of systems for its operation, many of which in turn require the use of electronic components, boards, and modules. Examples of such systems are those needed to ensure the necessary cryogenic and vacuum conditions required by

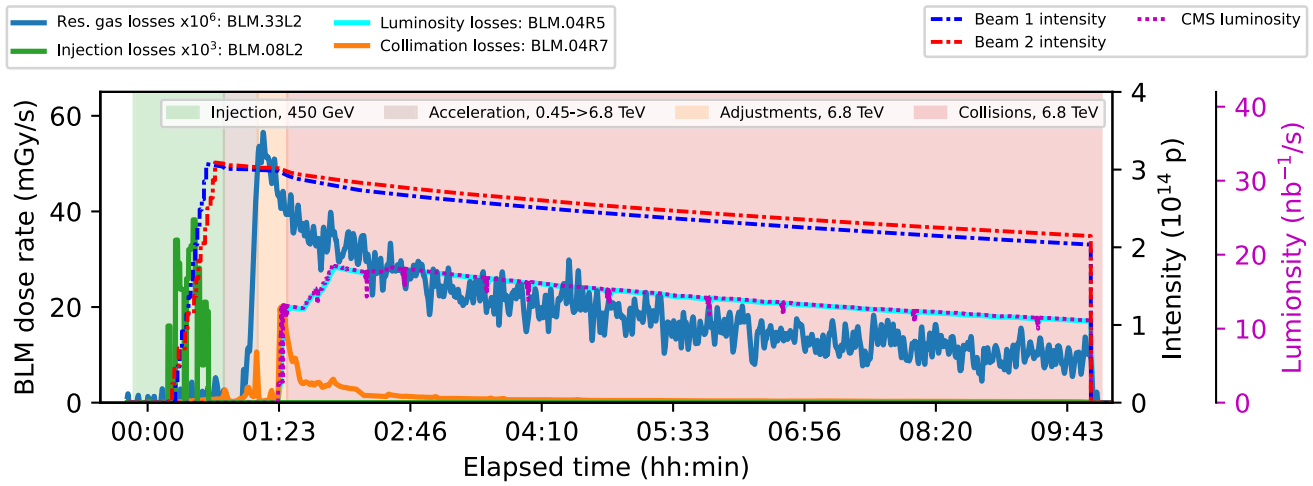

Fig. 3. Dose rate over the LHC fill #8228 measured by BLMs in the selected LHC regions, affected by the different beam loss mechanisms (due to injection, residual gas, collimation, and collisions), together with the CMS experiment luminosity, beam intensities, with highlighted accelerator state. The long-term TID evolution for the selected monitors is depicted in Fig. 5.

TABLE II
SELECTED STATISTICS OF THE LHC OPERATION IN 2018 AND IN 2022 [33], [34]

Quantity	2018	2022	unit	2022/2018 ratio
p+ energy	6.5	6.8	TeV	1.05
Duration with beam	141	101	days	0.72
incl. collisions only	79	44	days	0.55
Injected protons	15.0	13.5	10^{16} p	0.90
incl. collision fills only	10.7	6.7	10^{16} p	0.63
Dumped protons	11.5	11.0	10^{16} p	0.96
incl. collision fills only	7.4	4.8	10^{16} p	0.65
Protons lost due to luminosity burn-off	1.9	1.2	10^{16} p	0.63
Time-integrated intensity	30.6	17.9	10^{20} ps	0.58
incl. collision fills only	29.1	15.8	10^{20} ps	0.54
Lost in IR3 and IR7	1.6	1.3	10^{16} p	0.81
incl. collision fills only	1.3	0.64	10^{16} p	0.49
Total experiment integrated delivered luminosity	134	85	fb^{-1}	0.63
incl. CMS experiment	68	42	fb^{-1}	0.62

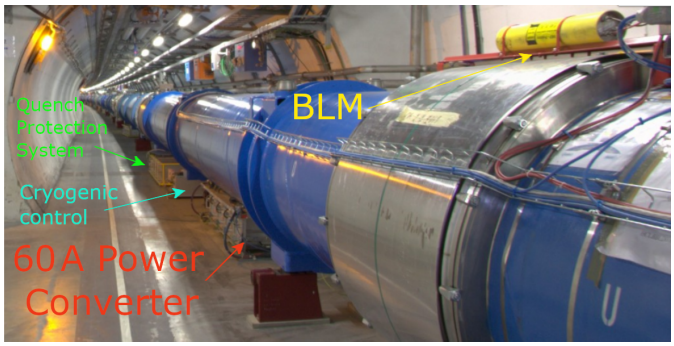

Fig. 4. Example of the electronic systems for: quench protection system, cryogenic control, and 60-A power converters with the FGClite controller; installed under the LHC beamlines, in the 18th half-cell on the left side of IR3. On top of the interconnect of the main dipole magnets, a BLM is installed.

the accelerator, the various types of magnets for beam bending and focusing, along with their powering and quench protection units [35], as well as beam instrumentation to ensure an

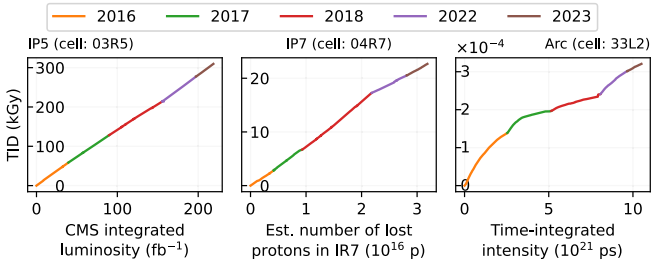

Fig. 5. Examples of TID evolution over: 1) CMS experiment integrated luminosity (left side); 2) the estimated number of lost particles in the collimation regions (center); and 3) time-integrated beam intensity; as measured by the BLMs in different locations of the LHC during 2016–2023 operation, illustrating the impact of different beam loss mechanisms (collision debris, collimation, and beam–residual gas interactions) on the TID measurements.

adequate beam quality and protect the machine from unwanted beam losses.

An example of the radiation-tolerant electronic racks installed in the LHC tunnel is illustrated in Fig. 4.

Both 60-A (installed in the arcs) and 120-A (installed in the RR-alcoves) Power Converters are controlled by FGClite modules [36], [37] featuring a 90-nm 8-Mbit Cypress SRAM (CY62157EV30LL-45ZSXI) onboard. This memory type is widely used for radiation-field characterization. The system performs the SEU readout daily, providing a number of SEU/MBU counts per day. The 752 units of 60-A-power-converter racks are installed along the LHC arc sectors, with four units installed in each half-cell, approximately 20 cm under the middle main bending dipoles, as depicted in Fig. 4. The other power converter racks (120 A, 600 A, 4 kA, 6 kA) equipped with FGClite, 256 units, are installed in the six RR shielded alcoves, both at the beamline level and at the RR's first floor. The radiation levels in the DS-regions could exceed the TID system tolerance [38]. Whereas the primary system objective is not radiation monitoring, as will be demonstrated, the SEUs recorded by the FGClite controllers provide distributed information concerning the relative radiation environment.

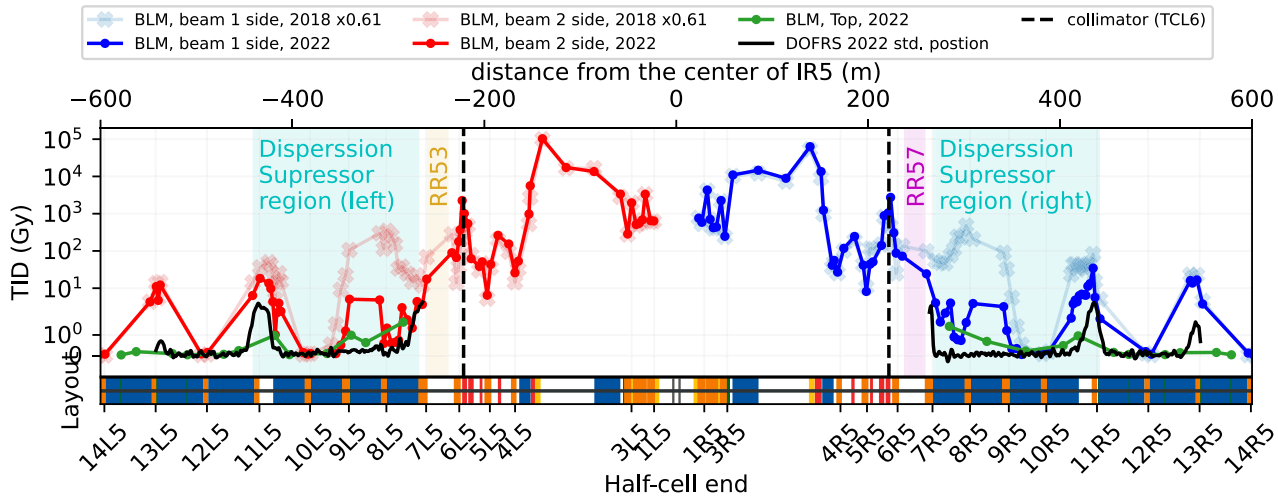

Fig. 6. TID levels in the IR5 (region of the CMS experiment, highlighted in Fig. 2), as measured in 2018 and 2022 by the BLMs. The smaller aperture of TCL6 collimators led to higher local losses (once normalized, increase in TID by a factor 20) and significant loss reduction in the half-cells of DSs (reduction in normalized TID over a factor 400). TID levels measured in 2018 were multiplied by a factor of 0.62 which is equal to the ratio of the integrated luminosities between 2022 and 2018.

III. Overview of the 2022 LHC Radiation Environment

Depending on the accelerator region, the beam loss mechanism behind the radiation varies. In the experimental IRs (and sometimes in the neighboring arcs), the dominant beam loss source is collision debris, which is lost or intercepted by collimators in the experimental IRs. In such regions, the dose rates scale with the luminosity of experiments. Examples of the dose rates measured in the various LHC locations, affected by different beam loss mechanisms, are depicted in Fig. 3. Close to the CMS experiment (or more generally the LHC experiments), dose rates scale with the respective experiment luminosity as they originate from the lost collision debris. In the long term, the related TID scales with the integrated luminosity of the experiment, as illustrated in Fig. 5. In the injection regions, the losses occur mostly during beam injections, at 450 GeV. Losses at the collimation region depend on the operation of the collimators (aperture) that might vary within an LHC fill. In the arc sectors, the losses are low and they rise during acceleration, with the increasing beam energy.

Another significant mechanism of beam loss is collimation, a procedure aiming at removing the particles that, due to scattering, do not meet the desired parameters. They are intercepted in these specially designed regions, such as in IR7 or IR3, that can withstand annual radiation levels of a few hundred Kilogray. For constant energy, the TID scaling in the collimation regions is, in first approximation, proportional to the number of protons that are intercepted, as depicted in Fig. 5.

In the arc sectors, the TID levels are driven by the interactions of the beam with residual gas molecules [39]. The levels are proportional to the residual gas density and the time-integrated beam intensity. As the residual gas density varies with time [40], the linearity between TID and time-integrated beam intensity is not preserved over long periods, as shown in Fig. 5.

A. Interaction Points

Radiation levels in the IRs are driven by the functionality of each region. In the case of experimental IRs (1, 2, 5, and 8), the dominant radiation sources are the off-momentum particles and collision debris that are intercepted by the collimators and other aperture restrictions, leading to the radiation showers.

Focusing on the IR5 that hosts the CMS experiment, a comparison between integrated luminosity-normalized TID levels measured by BLMs is presented in Fig. 6. In the regions less than 200 m away from the IR5 center, the normalized TID levels are fully comparable in 2018 and 2022. Then, around the TCL6 collimators, designed to intercept the collision debris and particle showers, the normalized TID levels increased up to a factor of 20 due to their tighter aperture. In 2018, these collimators were fully open (no beam interception) [41], whereas in 2022, they were closed to ± 25 mm, corresponding to 17σ in terms of beam size [42]. This affected radiation levels in the shielded alcoves RR57 (right side of IR5) and RR53, covered in Section III-D. Despite the local increase of the TID, there was a significant reduction in the DS regions (Section III-B), where multiple electronic systems are installed. A similar conclusion can be drawn for IR1, depicted in Fig. 7, where the ATLAS experiment is located.

As depicted in Fig. 8, the TID levels measured during collision time by BLMs in IR7, as a function of the protons lost at the collimator regions (IR7 and IR3) slightly decreased. This is also illustrated in Fig. 5. The comparison of the entire annual operation between 2018 and 2022 is not representative, as, during 2022, collimators have been extensively used due to recommissioning, for example, during scrubbing.

The ALICE region (IR2) is mainly dedicated to the operation involving heavy ions, and therefore, during standard p–p operation, the measured TID levels are low, below 260 Gy in 2022 BLM measurements. Moreover, IR2 is a region where Beam 1 is injected into the LHC.

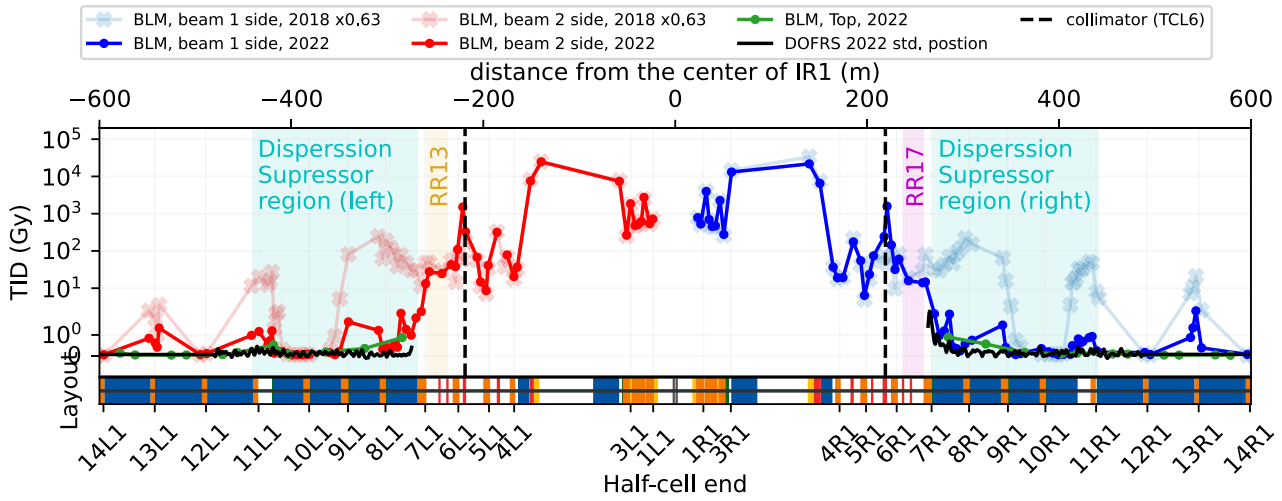

Fig. 7. TID levels in the IR1 (region of the ATLAS experiment), as measured in 2018 and 2022. The smaller aperture of TCL6 collimators leads to higher local losses (once normalized, increase in TID by a factor 20) and significant loss reduction in the half-cells of DSs (reduction in normalized TID over a factor 400). TID levels measured in 2018 were multiplied by a factor of 0.63 which is equal to the ratio of the integrated luminosities between 2022 and 2018.

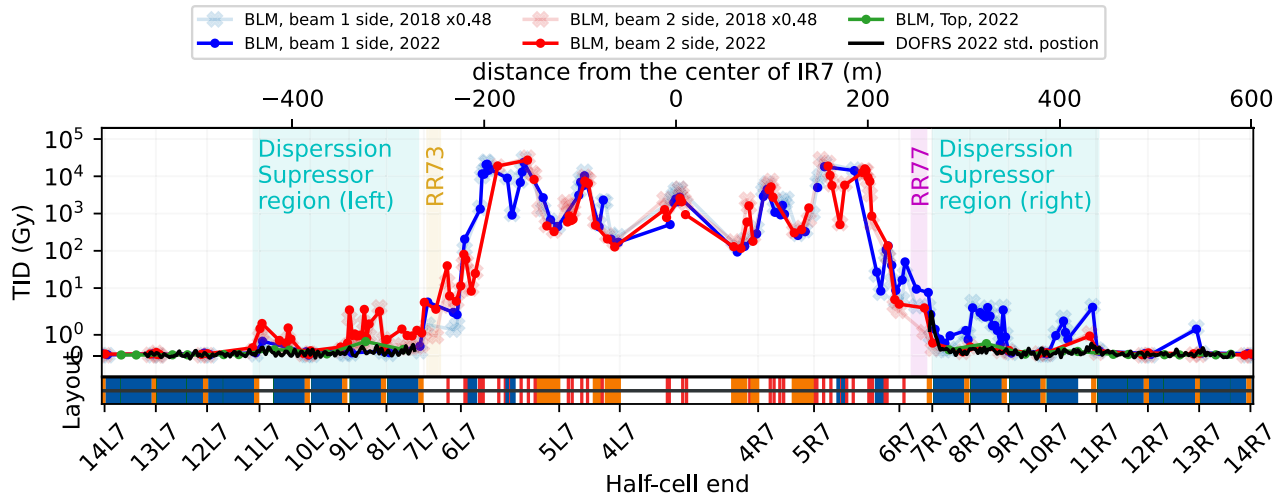

Fig. 8. TID levels in the IR7 (one of the collimation regions), as measured in 2018 and 2022 by BLMs during collision time. The smaller aperture of TCL6 collimators led to higher local losses (once normalized, increase in TID by a factor 20) and significant loss reduction in the half-cells of DSs (reduction in normalized TID over a factor 400). TID levels measured in 2018 were multiplied by a factor of 0.48 which is equal to the ratio of the integrated luminosities between 2022 and 2018.

The LHCb region (IR8) was upgraded during the LS2, aiming to increase the experiment luminosity (number of collisions) in Run 3. In 2022, no significant changes in TID profiles were observed. With the planned luminosity increase as of 2023, higher radiation levels are expected [43]. In addition to the experiment, IR8 is an injection region for Beam 2.

Losses in the remaining IRs are mainly caused by the accelerator systems necessary for the operation (e.g., collimators). In particular, in IR4, the dominant radiation source term is Beam Instrumentation [44], for example, Beam Gas Vertex demonstrator [45]. In 2022, in the sixth and seventh half-cells of the right side of IR4, an increase of up to factor 12 with respect to 2018 was observed, likely due to vacuum issues. IR6, a hosting beam dump system, the TID levels are mostly due to halo particles induced in IR7 [46]. No significant changes in the TID profile were observed, with the maximum increase within factor 1.7.

B. DSs: Experimental and Collimation Regions

DS regions are the first regions where radiation levels generally allow for the use of radiation-tolerant COTS-based custom electronics systems. The measured TID levels in the DS regions of IR1 and IR5 in 2022 were reduced by more than two orders of magnitude (x800 for a BLM with the highest reduction) with respect to 2018, as depicted in Fig. 6 due to the smaller aperture of TCL6 collimators that intercept the radiation showers created at the centers of IRs.

As of 2021, the DS regions of IR1, 5, and 7 have the DOFRS system installed. Due to the aforementioned reduction, TID levels as measured by the fiber are below 10 Gy, as depicted in Figs. 6–8. Focusing on the TID peak on the right side of IR5 (11th half-cell), Fig. 9 illustrates TID evolution during 2022 operation, when compared with the BLM monitor installed in the peak's proximity. The relative TID evolution for both sensors is in very good agreement. Moreover,

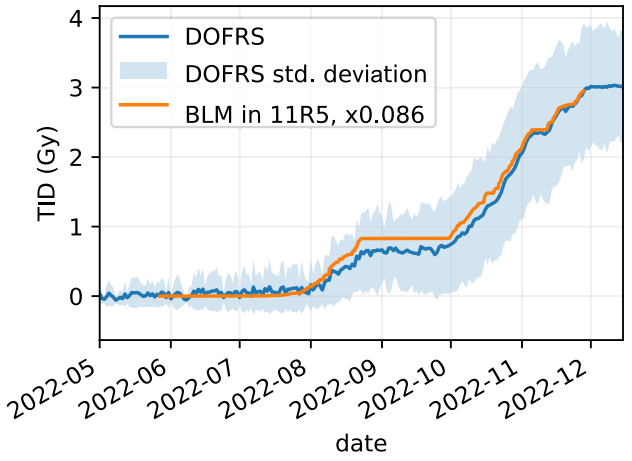

Fig. 9. Evolution of the TID over time as measured by the "top" BLM installed in the 11th half-cell of the right side of IR5 and by the DOFRS system at the same location (2 m spatial resolution, averaged between 13 764 m < dcum < 13 774 m).

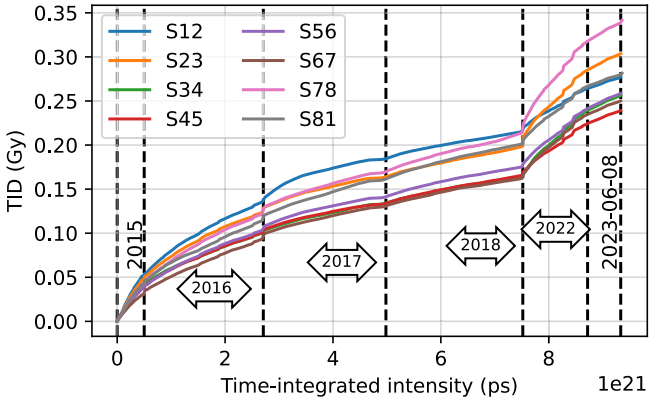

Fig. 10. Evolution of the baseline TID level as measured by top BLMs (installed on top of the dipole magnets) as a function of the time-integrated beam intensity for both beams (top energy only).

as depicted before, the DOFRS system covers partially IR1, IR5, and IR7, however, with varying lateral sensor positions, and therefore resulting in a more challenging TID profile to interpret.

C. Arc Sectors

In the LHC arc sections, the arrangement of both main magnets and radiation detectors is periodic. The expected dominant beam loss mechanism is inelastic interactions of the beam with residual gas molecules present in the vacuum chamber. As it was previously shown [44], the majority of the BLMs measured have similar, low TID levels. These baseline TID values are driven by the quality of the vacuum along the accelerator. Fig. 10 depicts the evolution of the typical (median) TID levels as a function of the time-integrated intensity per arc sector. Only one detector family, that is, having the same location with respect to a half-cell, was considered. In 2022, there is a factor 2.2 increase in the TID versus 2018, likely due to the worse vacuum quality after the LS2 (years 2019–2021). The trend observed in 2022 is, however, still similar to 2015, the first year after Long Shutdown 1 restart.

In addition to the long-term conditioning, within each LHC fill, a dynamic decrease of residual gas can be observed [40].

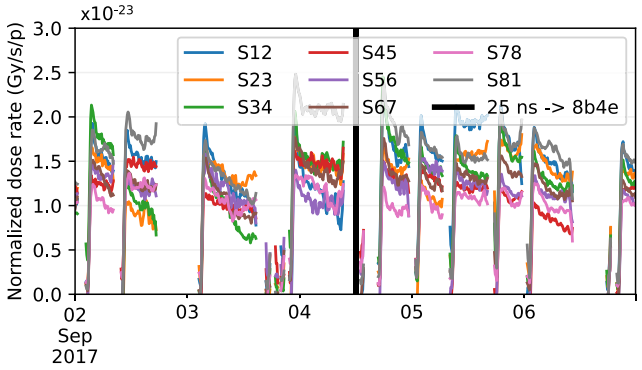

Fig. 11. Evolution of the baseline TID dose rate normalized to the beam intensity over several fills in September 2017. On 4 September, the accelerator-filling scheme was changed to reduce the impact of the e-cloud effect on the heat load of the cryogenic elements [47]. However, this change reduced the heat load by more than a factor 2, the baseline dose rates were not impacted, implying that the baseline dose rates are not impacted significantly by losses due to e-cloud.

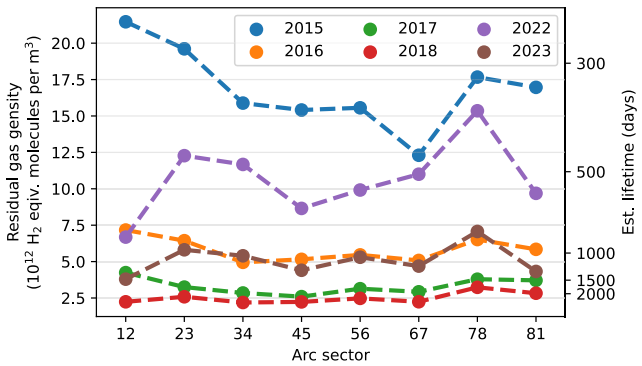

Fig. 12. Annual residual gas densities averaged per arc sectors, as retrieved indirectly through FLUKA Monte-Carlo simulations scaled to the TID measurements by top BLMs. The right y-axis represents the corresponding beam lifetime due to beam–residual gas interactions. Values for 2023 were retrieved based on the BLM data collected until 8 June 2022.

This is likely due to synchrotron radiation [48], which is proportional to the beam intensity. Another vacuum-related beam loss mechanism is an electron-cloud effect [49], limiting the total intensity that can be injected into the machine due to the heat load induced in the cryogenic elements. This effect was reduced with a change of a filling scheme; however, as depicted in Fig. 11, the change did not impact the measured baseline TID levels. Therefore, it is assumed that the e-cloud effect is not contributing significantly to the TID.

Similarly, as in the past studies [39], it is possible to indirectly retrieve the average annual residual gas density, by aligning the FLUKA simulations with the baseline BLM measurements. As depicted in Fig. 12, in 2022, the densities increased by factors 3–5 when compared to 2018's values. It is worth noting that, as opposed to Run 2, where arc 12 had the worst vacuum quality, in Run 3 arc 78 is the worst, factor 2 is worse with respect to arc 12 (that was the best 2022). In 2022, the beam lifetime (time after the intensity decreases by a factor e) due to beam–residual gas interactions would be in the order of a few hundred days. At the end of Run 2, this value was around 4–5 years. As anticipated, in 2023, the vacuum quality continues to improve, reaching 2016 values in June 2023.

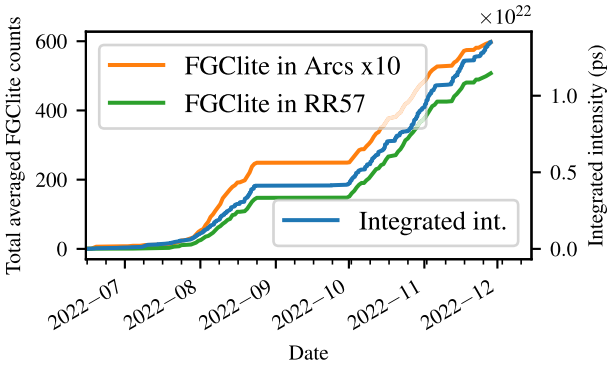

Fig. 13. Averaged and integrated SEU counts as registered by the FGClite controller of the power converters located in the RR57 and in the arcs (multiplied by a factor 10 for visibility), together with the time-integrated beam intensity. Without a dedicated radiation-tolerant design, a fraction of those events would have likely led to the R2E failures in the power converter system.

As depicted in Fig. 14, the degradation of the vacuum quality between 2018 and 2022 is reflected in the measurements from the FGClite controllers, distributed along the arc sections. The increase (median of the annual count of SEUs) of factor 3.5 between 2022 and 2018 is close to the TID increase (an arc median value from "top" detectors) as measured by BLMs, equal to factor 2.1. Additionally, consistently with BLM-driven measurements, arc sector 12 had the lowest median value of SEU counts, and arc 78 had the highest.

Despite low radiation levels in terms of cumulative damage, HEH fluences can be considered to be a significant source of SEEs, especially in distributed systems. However, in several locations, where other beam loss mechanisms dominate, the baseline TID levels are exceeded by up to three orders of magnitude [50].

D. RR-Shielded Alcoves

As of 2022, power converters installed in the RR-shielded alcoves are equipped with FGClite controllers, featuring SRAM capable of measuring SEUs. An example of such a measurement is depicted in Fig. 13, where the averaged evolution of the counts over time is illustrated. The trend, as expected, is similar to the evolution of the integrated intensity and the integrated luminosity.

As measured through the controllers and depicted in Fig. 14, in 2022, radiation levels in shielded alcoves around IR7 (RR73 and RR77) were similar to the one observed in arc sectors. However, in the RR-shielded alcoves close to high-luminosity experiments, IR1 and IR5, the measured number of SEUs was more than a factor 10 higher with respect to the arc environment. Controllers in the shielded alcoves of IR1 (RR13 and RR17) had a slightly lower number of SEUs when compared with RRs of IR5 (RR53, RR57), which is consistent with the TID measured in the DSs of that IRs (Figs. 6 and 7).

In addition, the shielded alcoves are often equipped with RadMons, further covered in Section III-E. For example, one of the monitors installed in the LHC tunnel, at the shielding wall of the RR57 alcove, registered an increase of a factor of 3.3, while comparing 2022 with 2018, in the normalized HEHeq levels, as depicted in Fig. 15. This is likely due to

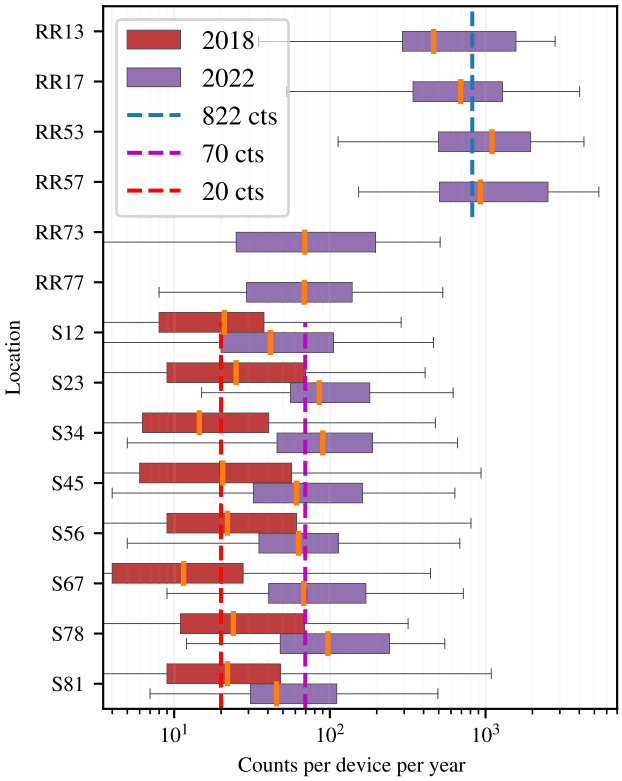

Fig. 14. Boxplot representation of the annual 2022 SEU counts measured by the FGClite controllers of the power converters installed along arc sectors (*SNM*) and in the shielded alcoves (RR*NM*). Each arc region (arc/RR) is represented by a box that spans between the first and the third quartiles, enclosing the middle 50% of measurements. The median value for each sector is denoted with orange bar and the whiskers correspond to the minimum/maximum measured value. Additionally, the median annual SEU count value for: 1) 2022 among racks in RR13/RR17/RR53/RR57; 2) 2018 among arc racks; and 3) 2022 among arc racks.

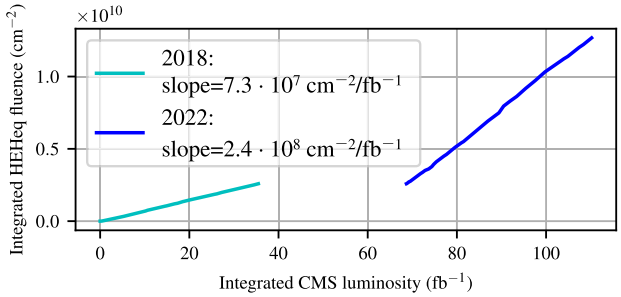

Fig. 15. Evolution of the HEHeq fluence measured by RadMon deployed in the LHC tunnel, at the wall of the RR57 shielded alcove, as a function of the integrated luminosity of the nearby experiment, that is, CMS. The change in the slope between 2018 and 2022 is caused by a tighter collimator aperture (TCL6), leading to higher local losses. The gap between the curves is due to the unavailability of the RadMon data at the end of the 2018 operation.

the aforementioned tighter aperture of collimators, leading to higher radiation levels in the vicinity of the shielded alcove.

E. High-Energy Hadron Fluence Measurements in the LHC: DSs, Arcs, and RRs

Underground areas at CERN, including those LHC-related, are equipped with RadMons. Fig. 16 illustrates the HEHeq fluence measurements, focusing on the detectors installed in the DS (8th <= half-cell < 12th) and arc (12th >= half-cell) regions of the LHC. Additionally, measurements from the 16 detectors installed close to RR-shielded alcoves are

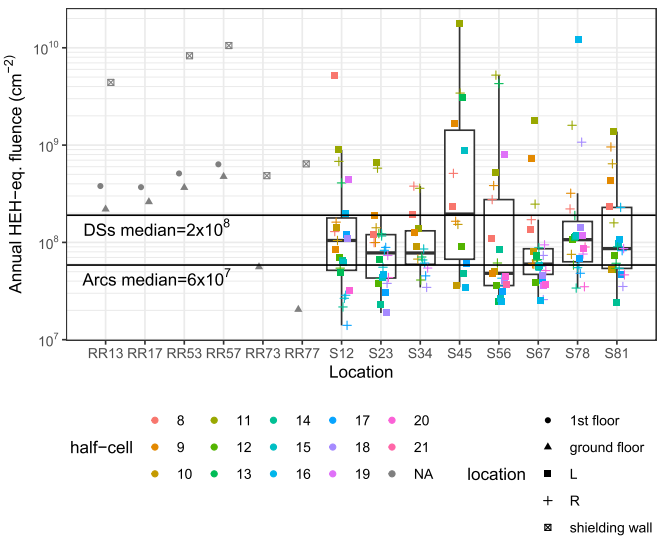

Fig. 16. Annual HEHeq fluence measured by the CERN RadMons in 2022, in the DS/arc half-cells of the LHC tunnel and its shielded alcoves (RRs). Color denotes a half-cell number and the marker type refers to the side of an IP, in the case of RadMons under LHC magnets. For example, 16R in S78 would correspond to RadMon in the half-cell 16R8. In the case of RR alcoves, the marker type refers to three possible locations: the ground/first floors of the alcove or the LHC tunnel wall (in the proximity of the alcove).

presented. In the arc sectors, RadMons are installed close to the main quadrupole magnets, below the beamline, whereas around the shielded alcoves RadMons are installed at three possible locations (shielding wall as well as ground and first floors of an alcove).

Among considered detectors, the highest annual HEHeq levels were measured in the LHC tunnel, at the shielding wall of the RR5X alcoves ($\sim 10^{10}$ cm^{-2}/year), in the 11th half-cell of the left side of IR5, and in the 16th half-cell of the left side of IR8. Median annual HEHeq measurement from the arc detectors is approximately equal to $6 \cdot 10^7$ cm^{-2}/year, factor $\sim$3 below the analogous value for monitors in the LHC DS regions.

Fig. 17 depicts the evolution of the averaged HEHeq fluence together with the rescaled averaged (per rack) SEU counts in arc 34. The relative evolution traces are in good agreement. The FGClite scaling factor, $8.5 \cdot 10^5$ cm^{-2}, can be interpreted as an inverse of the cross section that would make average FGClite fit average RadMon (in arc 34) and is equal to $\sigma = 1.2 \cdot 10^{-6}$ cm^2/device. Assuming only beam–residual gas-driven beam losses, the simulated HEHeq at the typical RadMon location is similar to the one at the FGClite location [39]. Therefore, one can compare σ with a measured cross section of the FGClite in the mixed-field $\sigma_{\text{FGClite}} = 2.35 \cdot 10^{-13} \cdot 8 \cdot 2^{20} = 2 \cdot 10^{-6}$ cm^2/device. The agreement is within 70%.

IV. RHA Implications

Given the large number of units and low TID levels along the machine, the main availability concern arises from the SEEs.

In the arc sectors, where multiple electronic systems are located (example in Fig. 4), the normalized radiation levels increased by a factor of 3–5 with respect to 2018.

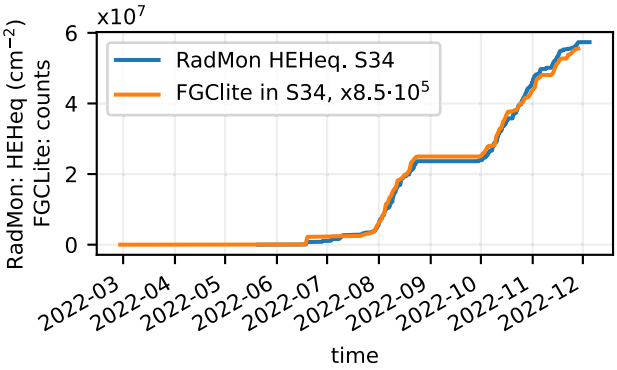

Fig. 17. Mean HEHeq fluence measured by the CERN RadMons, together with the evolution of the cumulative mean SEU counts by the FGClite controller, as measured in the arc sector 34 in 2022.

However, thanks to the power converter control radiation-tolerant development (FGClite) [36], [37], the increase did not lead to the R2E-induced beam dumps caused by the power converters. Moreover, it is expected that along the operation the vacuum conditions will improve, leading to the reduction of the baseline radiation levels. Apart from the typically low TID arc environment, there are some locations with locally increased loss levels [40], [50].

In the DS regions, the radiation levels were significantly reduced, leading to the increase of expected electronics lifetime, provided the same accelerator settings would be kept in the future. However, a consequence of the above is the increase in radiation levels in the RR-shielded alcoves. Before the FGClite deployment, the cross section of its predecessor was estimated to be $1.5–3 \cdot 10^{-10}$ cm^2/unit. In 2018, the old power converter controllers, installed in the shielded alcoves of both ATLAS and CMS experimental regions (RR13, RR17, RR53, and RR57), encountered 13 failures [5]. The corresponding annual measured HEHeq fluence, given by the RadMons in the shielded alcoves, was between 1.3 and $7.2 \cdot 10^8$ HEH/cm^2. The retrieved expected number of failures would be 9–22, in agreement with the observed value. If the FGClite had not been deployed, the expected failure rate would have been roughly factor 3 higher, following the increase depicted in Fig. 15.

The low R2E dump rate in 2022, illustrated in Fig. 1, was mainly a combination of the newly installed radiation-tolerant 600-A and 4–6–8-kA power converters in the RRs (no events), which were fully tested in CHARM, and whose predecessors were one of the main SEE contributors during Run 2 and the very low DS radiation levels, from which the equipment of the Quench Protection System, also an important Run 2 contributor, especially in 2018, strongly benefited. In 2022, the encountered R2E-related beam dumps were equally distributed systems (1–2 events), without a dominant contributor.

Overall, the LHC radiation hardness assurance (RHA) approach requires that whenever it is possible, the active electronic components, boards, and modules associated with such equipment are placed in radiation-safe areas. However, the civil engineering constraints of the accelerator infrastructure (notably the requirement of being built underground) in combination with cabling distance limits render the use of a fraction of such systems in radiation-exposed areas

TABLE III
APPROXIMATIVE R2E RADIATION LEVELS AND RELATED EFFECTS ON ELECTRONICS

HEH fl. (cm^{-2} yr^{-1})	TID for 10 yr (Gy)	Effects on Electronics
10^5	<<1	Possible SEE impact on commercial systems with many units and very demanding availability and reliability requirements
10^7	<1	SEE impact for systems with multiple units and demanding availability and reliability requirements
10^9	10	SEE mitigation (e.g. redundancy) at system level; cumulative effects can start to play a role
10^{11}	1000	SEE mitigation (e.g. redundancy) at system level, very challenging TID level for COTS
10^{15}	10^7	Rad-hard by design ASICs

unavoidable. And, such requirement of operating electronics in radiation-exposed areas, in combination with the availability needs of the various accelerator systems and accelerator as a whole, results in the necessity of designing and qualifying radiation tolerant systems, according to the expected radiation environment and related potential effects on electronics as listed in Table III.

V. CONCLUSION

This article gives an overview of the impact of radiation on electronic systems in the LHC. In particular, the RHA approach and the related radiation-tolerant designs lead to a significant decrease in the radiation-induced failures and hence the dump events per luminosity, with the 2022 value of $\leq$0.2 fb, being closer to the HL-LHC target (<0.1 fb).

Profiting from a variety of radiation monitors, such as BLMs and RadMons, we provided a detailed evaluation of the LHC radiation environment, a core ingredient of RHA.

The restart of the LHC in 2022 resulted in an increase in the arc radiation levels (70% of the accelerator) by a factor $\sim$3.5 with respect to 2018, due to the vacuum degradation during the shutdown period (2019–2021). It is expected that the situation will improve in the next years due to vacuum conditioning which can be observed for early 2023 measurements. This increase, however, is not a serious threat to the arcs' electronics as the developed systems are RHA-compliant (SEE redundancy).

Due to the different apertures of debris collimators around ATLAS and CMS regions, the TID levels in the DSs were reduced by more than two orders of magnitude. This, however, implied a localized increase of the levels in the collimator region (210 m away from the center of ATLAS/CMS experimental regions), and due to the spatial proximity, which in turn led to an increase in the RR shielded alcoves radiation levels, hosting multiple electronic racks.

Focusing on the analyzed LHC regions, the main RHA implications refer to the equipment installed in the RR alcoves, exposed to the collimator showers. This has been well understood and reproduced in simulations, and, therefore, several systems are undergoing radiation-hardening upgrades.

In the form of the SEE experiment, we presented SEU measurements from the power converter control boards featuring characterized SRAM memory. The measurements lead to similar conclusions (arc radiation increase and quality of different sectors) as drawn from the standard radiation monitors such as BLMs and highlight the very large number of SEEs that electronics in the accelerator encounter, underlining the importance of a radiation tolerant design and qualification.

Additionally, for the first time in the LHC, we demonstrated the capabilities of DOFRS for spatially continuous TID monitoring in the DSs of high-luminosity experimental regions (ATLAS and CMS) and the collimation (IR7) region.

ACKNOWLEDGMENT

The authors would like to thank the SY-BI-BL section for the support related to BLMs, Yves Thurel for providing information concerning the LHC Power Converters, Vincent Baglin for the insights into LHC vacuum, and Roderik Bruce for feedback concerning collimator openings.

REFERENCES

[1] L. Evans and P. Bryant, "LHC machine," *J. Instrum.*, vol. 3, no. 8, Aug. 2008, Art. no. S08001, doi: 10.1088/1748-0221/3/08/S08001.

[2] R. G. Alía et al., "LHC and HL-LHC: Present and future radiation environment in the high-luminosity collision points and RHA implications," *IEEE Trans. Nucl. Sci.*, vol. 65, no. 1, pp. 448–456, Jan. 2018.

[3] M. Brugger, "R2E and availability," in *Proc. LHC Perform. Workshop (Chamonix)*. Geneva, Switzerland: CERN, May 2015, pp. 149–160. [Online]. Available: https://cds.cern.ch/record/2020930

[4] S. Uznanski et al., "Qualification of electronic components for a radiation environment: When standards do not exist—High-energy physics," in *Proc. 17th Eur. Conf. Radiat. Effects Compon. Syst. (RADECS)*. Geneva, Switzerland: CERN, Oct. 2017, pp. 1–57. [Online]. Available: http://cds.cern.ch/record/2765495

[5] Y. Aguiar et al., "Radiation to electronics impact on CERN LHC operation: Run 2 overview and HL-LHC outlook," in *Proc. 12th Int. Part. Accel. Conf.* Geneva, Switzerland: JACOW Publishing, Aug. 2021, pp. 80–83. [Online]. Available: https://accelconf.web.cern.ch/ipac2021/doi/JACoW-IPAC2021-MOPAB013.html

[6] R. G. Alia et al., "SEU measurements and simulations in a mixed field environment," *IEEE Trans. Nucl. Sci.*, vol. 60, no. 4, pp. 2469–2476, Aug. 2013.

[7] D. D. Francesca et al., "Qualification and calibration of single-mode phosphosilicate optical fiber for dosimetry at CERN," *J. Lightw. Technol.*, vol. 37, no. 18, pp. 4643–4649, Sep. 15, 2019.

[8] K. Bilko et al., "CERN super proton synchrotron radiation environment and related radiation hardness assurance implications," *IEEE Trans. Nucl. Sci.*, vol. 70, no. 8, pp. 1606–1615, Aug. 2023.

[9] D. Di Francesca et al., "Distributed optical fiber radiation sensing in the proton synchrotron booster at CERN," *IEEE Trans. Nucl. Sci.*, vol. 65, no. 8, pp. 1639–1644, Aug. 2018.

[10] G. Apollinari et al., "High-luminosity large hadron collider (HL-LHC): Technical design report V. 0.1," CERN, Yellow, Geneva, Switzerland, Tech. Rep. CERN-2017-007-M, Sep. 2017. [Online]. Available: https://cds.cern.ch/record/2284929

[11] O. S. Bruning et al., "LHC design report," Monographs, CERN, Yellow, Geneva, Switzerland, Tech. Rep. CERN-2004-003-V-1, Jun. 2004.

[12] S. Chatrchyan et al., "The ATLAS experiment at the CERN large hadron collider," *J. Instrum.*, vol. 3, no. 8, Aug. 2008, Art. no. S08003, doi: 10.1088/1748-0221/3/08/S08003.

[13] S. Chatrchyan et al., "The CMS experiment at the CERN LHC," *J. Instrum.*, vol. 3, no. 8, Aug. 2008, Art. no. S08004, doi: 10.1088/1748-0221/3/08/S08004.

[14] K Aamodt et al., "The Alice experiment at the CERN LHC," *J. Instrum.*, vol. 3, no. 8, Aug. 2008, Art. no. S08002, doi: 10.1088/1748-0221/3/08/S08002.

[15] A. A. Alves et al., "The LHCb detector at the LHC," *J. Instrum.*, vol. 3, no. 8, Aug. 2008, Art. no. S08005, doi: 10.1088/1748-0221/3/08/S08005.

[16] S. Redaelli, "Beam cleaning and collimation systems," CERN, Yellow, Geneva, Switzerland, Yellow Rep. CERN-2016-002, vol. 2, p. 403, Jan. 2016. [Online]. Available: https://e-publishing.cern.ch/index.php/CYR/article/view/243

[17] D. Boussard et al., "The LHC superconducting cavities," in *Proc. Part. Accel. Conf.*, vol. 2. New York, NY, USA, Apr. 1999, pp. 946–948. [Online]. Available: http://ieeexplore.ieee.org/document/795409/

[18] R. Veness et al., "Development of a beam-gas curtain profile monitor for the high luminosity upgrade of the LHC," *Proc. 7th Int. Beam Instrum. Conf.*, Jan. 2019, pp. 472–476. [Online]. Available: http://jacow.org/ibic2018/doi/JACoW-IBIC2018-WEPB16.html

[19] B. Goddard et al., "Initial results from beam commissioning of the LHC beam dump system," in *Proc. 23rd Part. Accel. Conf. (PAC)*, Vancouver, BC, Canada, May 2009, pp. 1584–1586. [Online]. Available: https://cds.cern.ch/record/1199756/files/tu6rfp024.pdf

[20] E. Holzer et al., "Beam loss monitoring system for the LHC," in *Proc. IEEE Nucl. Sci. Symp. Conf. Rec.*, vol. 2, Oct. 2005, pp. 1052–1056.

[21] B. Dehning et al., "The LHC beam loss measurement system," in *Proc. IEEE Part. Accel. Conf. (PAC)*, Jun. 2007, pp. 4192–4194.

[22] E. B. Holzer et al., "Beam loss monitoring for LHC machine protection," *Phys. Proc.*, vol. 37, pp. 2055–2062, Jan. 2012. [Online]. Available: https://www.sciencedirect.com/science/article/pii/S1875389212019281

[23] B. Dehning et al., "LHC beam loss detector design: Simulation and measurements," in *Proc. IEEE Part. Accel. Conf. (PAC)*, Jun. 2007, pp. 4198–4200.

[24] K. Biłko et al., "Automated analysis of the prompt radiation levels in the CERN accelerator complex," in *Proc. 13th Int. Part. Accel. Conf. (IPAC)*. Bangkok, Thailand: JACOW, Jul. 2022, pp. 736–739. [Online]. Available: https://accelconf.web.cern.ch/ipac2022/doi/JACoW-IPAC2022-MOPOMS043.html

[25] O. Stein et al., "A systematic analysis of the prompt dose distribution at the large hadron collider," in *Proc. 9th Int. Part. Accel. Conf. (IPAC)*. Vancouver, BC, Canada: JACOW, Jun. 2018, pp. 2036–2038. [Online]. Available: https://accelconf.web.cern.ch/ipac2018/doi/JACoW-IPAC2018-WEPAF082.html

[26] G. Spiezia et al., "The LHC radiation monitoring system—RadMon," *Proc. Sci.*, vol. RD11, p. 24, Oct. 2012.

[27] G. Spiezia et al., "A new Radmon version for the LHC and its injection lines," *IEEE Trans. Nucl. Sci.*, vol. 61, no. 6, pp. 3424–3431, Dec. 2014.

[28] M. Cecchetto et al., "0.1–10 MeV neutron soft error rate in accelerator and atmospheric environments," *IEEE Trans. Nucl. Sci.*, vol. 68, no. 5, pp. 873–883, May 2021.

[29] M. Cecchetto et al., "Thermal neutron-induced SEUs in the LHC accelerator environment," *IEEE Trans. Nucl. Sci.*, vol. 67, no. 7, pp. 1412–1420, Jul. 2020.

[30] D. D. Francesca et al., "Dosimetry mapping of mixed-field radiation environment through combined distributed optical fiber sensing and FLUKA simulation," *IEEE Trans. Nucl. Sci.*, vol. 66, no. 1, pp. 299–305, Jan. 2019.

[31] D. Di Francesca et al., "Radiation-induced attenuation in single-mode phosphosilicate optical fibers for radiation detection," *IEEE Trans. Nucl. Sci.*, vol. 65, no. 1, pp. 126–131, Jan. 2018.

[32] M. Lamont, "Estimates of annual proton doses in the LHC," CERN, Geneva, Switzerland, Tech. Rep. CERN-LHC-Project-Note-375, Jun. 2005. [Online]. Available: http://cds.cern.ch/record/893060

[33] K. Biłko and O. Stein, "Report on the prompt dose distribution along the LHC based on BLM data for proton-proton operation in run 2," CERN, Geneva, Switzerland, Tech. Rep. CERN-ACC-NOTE-2019-0040, Sep. 2019.

[34] The CMS Collaboration. (Jul. 2023). *Delivered Luminosity Versus Time for 2015-2018 and 2022-2023 (PP Data Only)*. [Online]. Available: https://twiki.cern.ch/twiki/bin/view/CMSPublic/LumiPublicResults#2022_proton_proton_collisions_at

[35] R. Denz, E. de Matteis, A. Siemko, and J. Steckert, "Next generation of quench detection systems for the high-luminosity upgrade of the LHC," *IEEE Trans. Appl. Supercond.*, vol. 27, no. 4, pp. 1–4, Jun. 2017.

[36] B. Todd, A. Dinius, Q. King, and S. Uznanski, "Radiation tolerant power converter controls," *J. Instrum.*, vol. 7, no. 11, Nov. 2012, Art. no. C11012.

[37] S. Uznanski, B. Todd, A. Dinius, Q. King, and M. Brugger, "Radiation hardness assurance methodology of radiation tolerant power converter controls for large hadron collider," *IEEE Trans. Nucl. Sci.*, vol. 61, no. 6, pp. 3694–3700, Dec. 2014.

[38] S. Uznanski et al., "Qualification of electronic systems for radiation environments of high energy accelerator," in *Proc. 25th Int. Conf. Mixed Des. Integr. Circuits Syst.*, Jun. 2018, pp. 34–38.

[39] K. Bilko et al., "Radiation environment in the LHC arc sections during run 2 and future HL-LHC operations," *IEEE Trans. Nucl. Sci.*, vol. 67, no. 7, pp. 1682–1690, Jul. 2020.

[40] K. Bilko et al., "Overview of total ionizing dose levels in the large hadron collider during 2022 restart," in *Proc. 14th Int. Part. Accel. Conf. (IPAC)*. Geneva, Switzerland: JACoW Publishing, May 2023, pp. 4008–4011. [Online]. Available: https://indico.jacow.org/event/41/contributions/2667

[41] N. F. Martinez et al., "Run 2 collimation overview," in *Proc. 9th Evian Workshop LHC Beam Operation*. Evian Les-Bains, France: CERN, Feb. 2019, pp. 149–164. [Online]. Available: https://cds.cern.ch/record/2750291

[42] D. Mirarchi et al. (Apr. 2022). *Collimator Setting Strategy for 2022 Commissioning and Run*. [Online]. Available: https://indico.cern.ch/event/1147643/contributions/4817101/attachments/2425091/4186876/CollSettings_DM.pdf

[43] A. Ciccotelli et al., "Energy deposition studies for the LHCb insertion region of the CERN large hadron collider," *Phys. Rev. Accel. Beams*, vol. 26, no. 6, Jun. 2023, Art. no. 061002, doi: 10.1103/PhysRevAccelBeams.26.061002.

[44] K. Bilko and R. G. Alia. (May 2020). *Overview of Radiation Levels in IR4*. [Online]. Available: https://zenodo.org/record/8253071

[45] D. Prelipcean et al., "Radiation levels produced by the operation of the beam gas vertex monitor in the LHC tunnel at IR4," in *Proc. 14th Int. Part. Accel. Conf. (IPAC)*. Geneva, Switzerland: JACoW Publishing, May 2023, pp. 4578–4581. [Online]. Available: https://indico.jacow.org/event/41/contributions/2501

[46] J.-B. Potoine et al., "Risk of halo-induced magnet quenches in the HL-LHC beam dump insertion," in *Proc. 12th Int. Part. Accel. Conf.*, Aug. 2021, pp. 1–4. [Online]. Available: https://jacow.org/ipac2021/doi/JACoW-IPAC2021-MOPAB002.html

[47] J. Wenninger. (Sep. 2017). *LHC Report: Operation With Holes*. [Online]. Available: https://home.cern/news/news/accelerators/lhc-report-operation-holes

[48] V. Baglin et al., "Synchrotron radiation in the LHC vacuum system," in *Proc. 2nd Int. Part. Accel. Conf. (IPAC)*, San Sebastian, Spain, Sep. 2011, pp. 1–3. [Online]. Available: https://accelconf.web.cern.ch/IPAC2011/papers/TUPS019.pdf

[49] P. Chiggiato et al., "Observations of electron cloud effects with the LHC vacuum system," in *Proc. 2nd Int. Part. Accel. Conf. (IPAC)*, San Sebastian, Spain, Sep. 2011, pp. 1560–1562. [Online]. Available: https://accelconf.web.cern.ch/ipac2011/papers/tups018.pdf

[50] K. Bilko et al., "Detailed analysis of the baseline dose levels and localized radiation spikes in the arc sections of the large hadron collider during run 2," in *Proc. 10th Int. Part. Accel. Conf. (IPAC)*. Melbourne, VIC, Australia: JACOW Publishing, Jun. 2019, pp. 4009–4012. [Online]. Available: https://accelconf.web.cern.ch/ipac2019/doi/JACoW-IPAC2019-THPRB083.html